7-2010

Polar Mesospheric Cloud Structures Observed From the Cloud Imaging and Particle Size Experiment on the Aeronomy of Ice in the Mesosphere Spacecraft: Atmospheric Gravity Waves as Drivers for Longitudinal Variability in Polar Mesospheric Cloud Occurrence

A. Chandran

D. W. Rusch

A. W. Merkel

S. E. Palo

G. E. Thomas

Michael J. Taylor
Utah State University

See next page for additional authors

JOURNAL OF GEOPHYSICAL RESEARCH, VOL. 115, D13102, doi:10.1029/2009JD013185, 2010

Polar mesospheric cloud structures observed from the cloud imaging and particle size experiment on the Aeronomy of Ice in the Mesosphere spacecraft: Atmospheric gravity waves as drivers for longitudinal variability in polar mesospheric cloud occurrence

A. Chandran,[1,2] D. W. Rusch,[1] A. W. Merkel,[1] S. E. Palo,[2] G. E. Thomas,[1] M. J. Taylor,[3] S. M. Bailey,[4] and J. M. Russell III[5]

Received 11 September 2009; revised 3 December 2009; accepted 22 January 2010; published 8 July 2010.

[1] The cloud imaging and particle size (CIPS) experiment is one of three instruments on board the Aeronomy of Ice in the Mesosphere (AIM) spacecraft that was launched into a 600 km Sun-synchronous orbit on 25 April 2007. CIPS images have shown distinct wave patterns and structures in polar mesospheric clouds (PMCs), around the summertime mesopause region, which are qualitatively similar to structures seen in noctilucent clouds (NLCs) from ground-based photographs. The structures in PMC are generally considered to be manifestations of upward propagating atmospheric gravity waves (AGWs). Variability of AGW effects on PMC reported at several lidar sites has led to the notion of longitudinal differences in this relationship. This study compares the longitudinal variability in the CIPS-observed wave occurrence frequency with CIPS-measured PMC occurrence frequency and albedo along with mesospheric temperatures measured by the sounding of the atmosphere using broadband emission radiometry instrument on board the Thermosphere Ionosphere Mesosphere Energetics and Dynamics spacecraft. Our results for the latitude ranges between 70° and 80° show a distinct anticorrelation of wave structures with cloud occurrence frequency and correlations with temperature perturbations for at least two of the four seasons analyzed, supporting the idea of gravity wave-induced cloud sublimation. The locations of the observed wave events show regions of high wave activity in both hemispheres. In the Northern Hemisphere, while the longitudinal variability in observed wave structures show changes from the 2007–2008 seasons, there exist regions of both low and high wave activities common to the two seasons. These persistent features may explain some of the observed differences in PMC activity reported by ground-based lidar instruments distributed at different longitudes. The statistical distribution of horizontal scales increases with wavelength up to at least 250 km. We also discuss the possibility of atmospheric tides, especially the nonmigrating semidiurnal tide, aliasing our observations and affecting the results presented in this analysis.

Citation: Chandran, A., D. W. Rusch, A. W. Merkel, S. E. Palo, G. E. Thomas, M. J. Taylor, S. M. Bailey, and J. M. Russell III (2010), Polar mesospheric cloud structures observed from the cloud imaging and particle size experiment on the Aeronomy of Ice in the Mesosphere spacecraft: Atmospheric gravity waves as drivers for longitudinal variability in polar mesospheric cloud occurrence, *J. Geophys. Res.*, *115*, D13102, doi:10.1029/2009JD013185.

1. Introduction

[2] Noctilucent clouds (NLCs) or polar mesospheric clouds (PMCs) as they are known from space-based observations form in the cold summer mesopause region. This region is cooler than the winter mesopause region by about 90 K, with mean temperatures between ~128 K at the mesopause and 150 K at 82 km [*Lübken*, 1999]. For the pressure range representative of the mesopause, this is an environment suitable for water ice formation. *Rapp and Thomas* [2006] provided a review of the microphysics of PMC and a model study describing a high sensitivity of PMC properties to tempera-

[1]Laboratory for Atmospheric and Space Physics, University of Colorado, Boulder, Colorado, USA.
[2]Department of Aerospace Engineering, University of Colorado, Boulder, Colorado, USA.
[3]Center for Atmospheric and Space Sciences and Physics Department, Utah State University, Logan, Utah, USA.
[4]Bradley Department of Electrical and Computer Engineering, Virginia Polytechnic Institute and State University, Blacksburg, Virginia, USA.
[5]Center for Atmospheric Sciences, Hampton University, Hampton, Virginia, USA.

0148-0227/10/2009JD013185

ture. Since the pioneering work of *Hines* [1968], atmospheric gravity waves (AGWs) have been known to be the main cause of extensive band structures often evident in NLC. AGWs are even more important in their role as the driver for the cold summer mesopause temperatures. AGW disturbances mainly originate in the lower atmosphere and propagate upward, growing in amplitude because of decreasing atmospheric density, eventually becoming unstable and breaking in the upper atmosphere. The generally accepted theory is that the momentum deposited during this process profoundly influences the mean zonal circulation pattern in the upper atmosphere, opposite to that expected from radiative equilibrium. This in turn forces a residual mean meridional circulation, upwelling, and an adiabatic cooling that leads to the cold summer mesopause [*Leovy*, 1964; *Holton*, 1983].

[3] NLC often display distinct small-scale wave patterns termed billows, with horizontal spacing of ~3 to 10 km) while the larger-scale bands exhibit horizontal wavelengths typically >30 km [*Witt*, 1962; *Haurwitz and Fogle*, 1969; *Gadsden and Parviainen*, 1995]. *Hines* [1968] first proposed that structures seen in NLC were the manifestation of AGW. Later modeling work by *Fritts et al.* [1993] has also suggested that some small-scale mesospheric structures are likely secondary waves originating in breaking AGW. The issue we address in this paper is the effect of these waves on PMC resulting in an apparent longitudinal variability in PMC occurrences which is driven by a longitudinal variability in AGW activity.

[4] *Turco et al.* [1982] first developed a 1-D version of the community aerosol and radiation model for atmospheres (CARMA) model for NLC formation that included the effect of AGW-induced temperature variations. *Jensen and Thomas* [1994] and subsequently *Rapp et al.* [2002] have used multidimensional version of the CARMA model to investigate the effect of large-scale monochromatic AGW on PMC formation and evolution. *Turco et al.* [1982] and *Jensen and Thomas* [1994] found that the net effect of wave-induced temperature perturbations is to decrease the cloud albedo, since ice sublimation is much more rapid than ice crystal growth. They also proposed that mean mesopause temperatures must be about 5 K colder for PMC to form in the presence of AGW than in their absence. *Rapp et al.* [2002], using an updated version of the Jensen and Thomas model, showed that AGW with periods longer than 6.5 h can temporarily amplify PMC brightness while shorter-period waves produce the opposite effect. Using rocket sounding measurements, they also showed that wave-associated temperature fluctuations as high as 6 K, 10 K, and 20 K are present at altitudes of 80, 85, and 95 km, respectively.

[5] *Hecht et al.* [1997] provided observational evidence of wave-induced sublimation in PMC from lidar measurements made at Söndrestrom, Greenland. *Gerrard et al.* [1998, 2004] and *Thayer et al.* [2003] provided evidence from lidar measurements at Söndrestrom (67°N), that short-period AGW activity in the stratosphere is inversely proportional to PMC backscattering. *Thayer et al.* [2003] also reproduced the measured weaker PMC backscatter and thinner clouds using CARMA modeling which included short-period AGW. Conversely, it should be noted that similar lidar measurements above Kühlungsborn (54°N), Germany [*Gerding et al.*, 2007]; Alomar (69.3°N), Norway [*Schöch*, 2007]; and Davis (68.6°S), Antarctica [*Innis et al.*, 2008], showed no significant correlation between PMC brightness and stratospheric AGW activity. *Chu et al.* [2009] have shown through lidar observations that PMC brightness is negatively correlated with stratospheric AGW strength at Rothera (67.5°S) while no significant correlation was found at the South Pole (90°S).

[6] That an intimate relationship exists between AGW-associated temperature variations and PMC have been suspected for years, yet a detailed understanding of the relationship is still lacking. The discrepancies of the PMC/AGW correlations between fixed lidar sites suggest that longitudinal/latitudinal differences in the character of AGW may be responsible. Ground-based studies provide valuable "snapshots, " but what is needed are global scale measurements, possible only from space-based platforms. The 5 × 5 km resolution images from the CIPS experiment, operating on the Aeronomy of Ice in the Mesosphere (AIM) satellite [*Russell et al.*, 2009], are taken daily over the entire polar cap and can provide the new information to study these interactions, since they resolve most of the wave structures that affect PMC. *Thomas and Olivero* [1989] investigated longitudinal variability in PMC from the Solar Mesospheric Explorer (SME) data but found no significant large-scale variations at latitudes poleward of 70° where SME had 65% or more coverage. In the following sections we analyze CIPS images to search for periodic structures in the PMC data during the 2007–2008 summer seasons. In section 2 we provide an overview of the CIPS and sounding of the atmosphere using broadband emission radiometry (SABER) instruments. In section 3 the wave detection algorithm and its limitations as well as the selection of the latitude region for analysis are presented. We present results demonstrating the existence of longitudinal variability in the occurrence of these periodic structures and show anticorrelations between this variability and cloud properties measured by CIPS in section 4. We also show correlations with temperature measurements made from the SABER experiment at PMC altitudes. In section 5 we discuss the possible causes for the longitudinal variations in AGW activity and temperature and their effects on PMC formation and evolution that can cause the large-scale variations observed by CIPS.

2. Observations

2.1. CIPS

[7] The CIPS instrument [*McClintock et al.*, 2009] consists of four UV nadir imager cameras that image the Earth's albedo with a band pass centered at 265 nm and extending from 258 to 274 nm (half-power points). The four CIPS cameras have an overlapping field of view of 120° (along orbit track) × 80° (cross orbit track). The details of the CIPS instruments, camera configuration, and first results are given by *Rusch et al.* [2009]. The four CIPS camera images are merged to form a single image that is referred to as a "scene" that has the shape of a bow tie when projected onto a spherical Earth surface. CIPS cameras take an image every 43 s with an exposure time of ~1 s. On average, each CIPS camera takes 26 images per orbit over the sunlit summer polar region. The analysis of wave structures in this paper uses images only from the most sunward viewing camera.

[8] The pixels constituting a scene have a best resolution of 1 × 2 km in the nadir. Data used in this study are averaged to give a spatial resolution of ~5 × 5 km throughout the entire

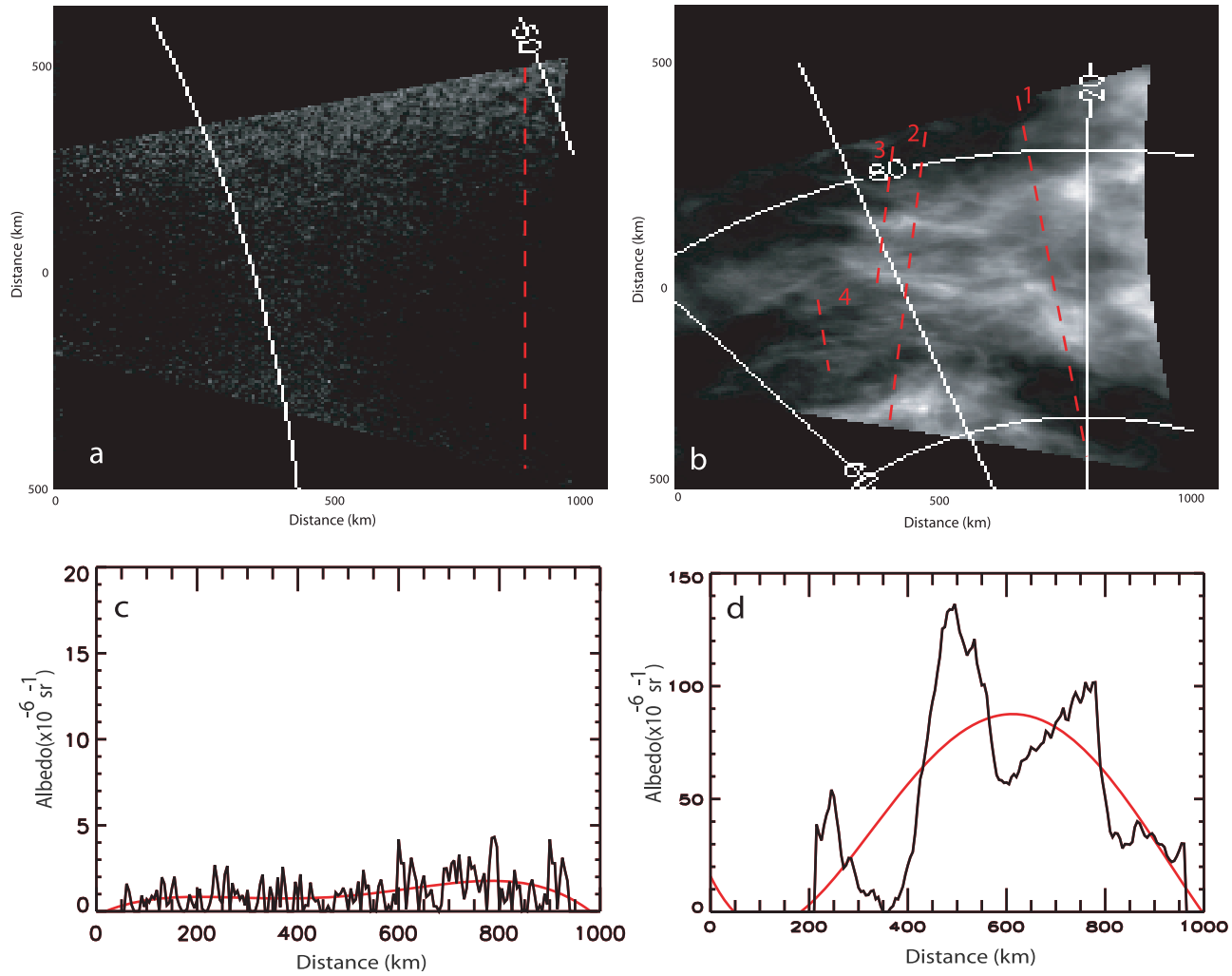

Figure 1. CIPS forward camera images in gray scale with the background scattering removed. (a) CIPS image taken 50°N at the start of the PMC season on 28 May. (b) CIPS image taken on 17 July at 80°N showing multiple PMC structures. The white lines are contour lines for longitude and latitude. (c) Plot showing albedo values along a trace (denoted by dashed red line) and polynomial fit made to the data in solid red through the image in Figure 1a. (d) Plot showing the albedo along a trace 1, orthogonal to the wavefront (denoted by dashed red line), and polynomial fit made to a trace through the wave field in Figure 1b.

scene. In CIPS images, Rayleigh scattering from the atmosphere constitutes a bright background, and PMCs are seen as enhancements in the background albedo because of scattering from the ice cloud particles. Therefore, accurate removal of the Rayleigh scattered background is a critical aspect of the data processing needed for cloud detection. The Rayleigh scattered background varies across the scene as a result of changes in both scattering and viewing angles [*Rusch et al.*, 2009]. *Bailey et al.* [2009] describe in detail a technique for separation of PMC and Rayleigh radiances in CIPS observations.

[9] A description of the various CIPS data products is available online from the AIM Web site at http://aim.hamptonu.edu/library/documentation/instruments/cips/cips_docs.html. The data used in this analysis for AGW detections are the level 1c format, and the cloud occurrence frequencies are derived from the level 4 format. We have normalized the albedo of the level 1c data used in this analysis for scattering angle of 90° and a nadir (0°) view angle. This is accomplished by removing the sec (θ) geometry factor to account for the view angle dependence and by assuming a Gaussian particle size distribution with effective radius 60 nm and 14 nm half width to account for the scattering angle dependence. This assumption follows that of *Rusch et al.* [2009]. *McClintock et al.* [2009] describe the flat fielding and calibration of the CIPS images. Figures 1a and 1b are examples of two CIPS images with the Rayleigh background removed. Figure 1a is an image taken at low latitude where no clouds are present. The albedo values along a trace taken through the image, denoted by the dashed red line in Figure 1a, and the polynomial fit to the cloud albedo (in red) is plotted in Figure 1c. Figure 1b is an image of PMC that contain multiple periodic structures. Four columnwise numbered traces denoted by red dashed lines are used to derive the horizontal scales of the wave structures present in the image. The cloud albedo and polynomial fit made to the albedo, along the longest trace, near the right edge of the image, and denoted by "1" is plotted in Figure 1d. A comparison of the

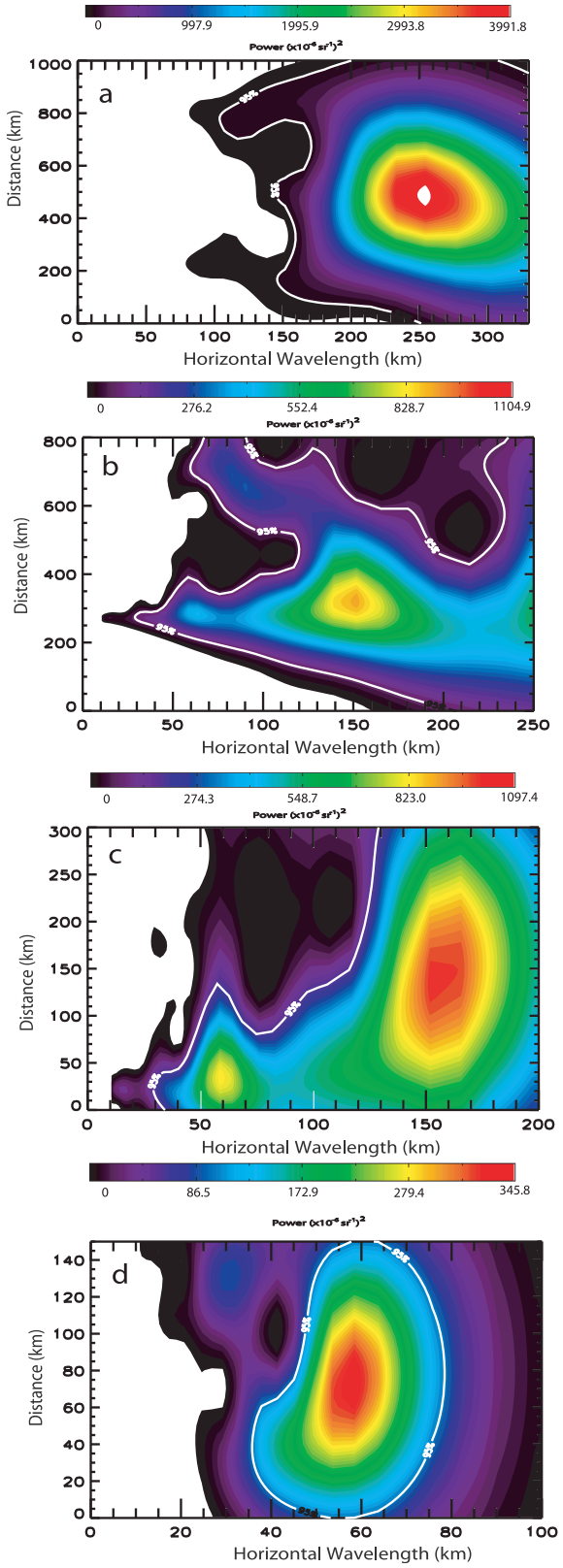

Figure 2. Four-panel plot showing wavelet power spectrum of the residual from the traces in Figure 1b along (a) trace 1 having horizontal wavelength at 255 km, (b) trace 2 having multiple waves with horizontal wavelength at ~150 km and ~60 km, (c) trace 3 having horizontal wavelength at 158 km, and (d) trace 4 having horizontal wavelength at 57 km.

albedo values in Figures 1c and 1d illustrate the quality of the background removal and flat fielding. We will provide an analysis of the wave structures in Figure 1b in section 3 and Figure 2. The forward camera images are used to maximize PMC detection capability, because of the strong forward-scattering behavior of PMC ice particles [*Bailey et al.*, 2009].

2.2. SABER

[10] SABER is one of four instruments onboard the Thermosphere Ionosphere Mesosphere Energetics and Dynamics (TIMED) satellite launched in December 2001 [*Russell et al.*, 1999]. It is a 10-channel infrared limb-scanning radiometer that produces altitude profiles of temperature, chemistry, and energetics parameters with 2 km vertical resolution every 58 s over the range from ~180 km down to the upper tropopause. The analysis presented here is given by *Merkel et al.* [2009] and uses SABER v1.07 temperature data that have been validated to a level of ~2 to 3 K [*Remsberg et al.*, 2008]. Since temperature perturbations are being used for the analysis in this paper as opposed to absolute values, the effects of any temperature biases in the SABER results will be negligible. The latitudes viewed by SABER cover the ranges from 52°S to 83°N and from 83°S to 52°N. Because the TIMED satellite orbit precesses by ~3°/day, the spacecraft must perform a yaw maneuver every ~63 days in order for the SABER detectors to avoid viewing the Sun. Unfortunately, the yaw maneuver occurs in the middle of the PMC season (provides data from about 35 days before solstice to about 25 days after) in each hemisphere. This results in the availability of continuous temperature data only from before the start to the middle of the PMC season. The observations presented in this paper are for 20–25 day periods centered around solstice in each hemisphere. SABER measurements cover all local time (LT) through this period.

3. Wave Detection Technique

[11] An initial wave analysis technique for detection of AGW structure in CIPS PMC images was presented by *Chandran et al.* [2009]. The technique consisted of first visually identifying quasi monochromatic wave structures in PMC, similar to structures seen from ground-based observations of NLC. *Chandran et al.* [2009] show examples of CIPS images with distinct wave structures in PMC similar to Figure 1b. In this paper, we present results using an automated wave searching routine to detect periodic structures in CIPS PMC images. Section 3 describes the steps involved in the wave detection process that is depicted in the form of a flowchart in Figure 3.

[12] Traces across the camera image, which correspond to the entire columns of pixels across the track of the orbit, are analyzed systematically for periodic structures. This is done for every column and 10 equally spaced rows in the camera image. The first stage in the wave detection process is to fit a fourth-order polynomial to the cloud data along the entire trace to estimate the underlying smooth PMC field. Periodic perturbations from this smooth cloud field are considered to be caused by wave structures in the PMC. The result of this polynomial fit is to act as a low-pass filter, which is subtracted from the PMC data leaving only the periodic structures [see *Chandran et al.*, 2009]. As described in section 2, Figure 1d shows the albedo values and the fourth-order polynomial fit

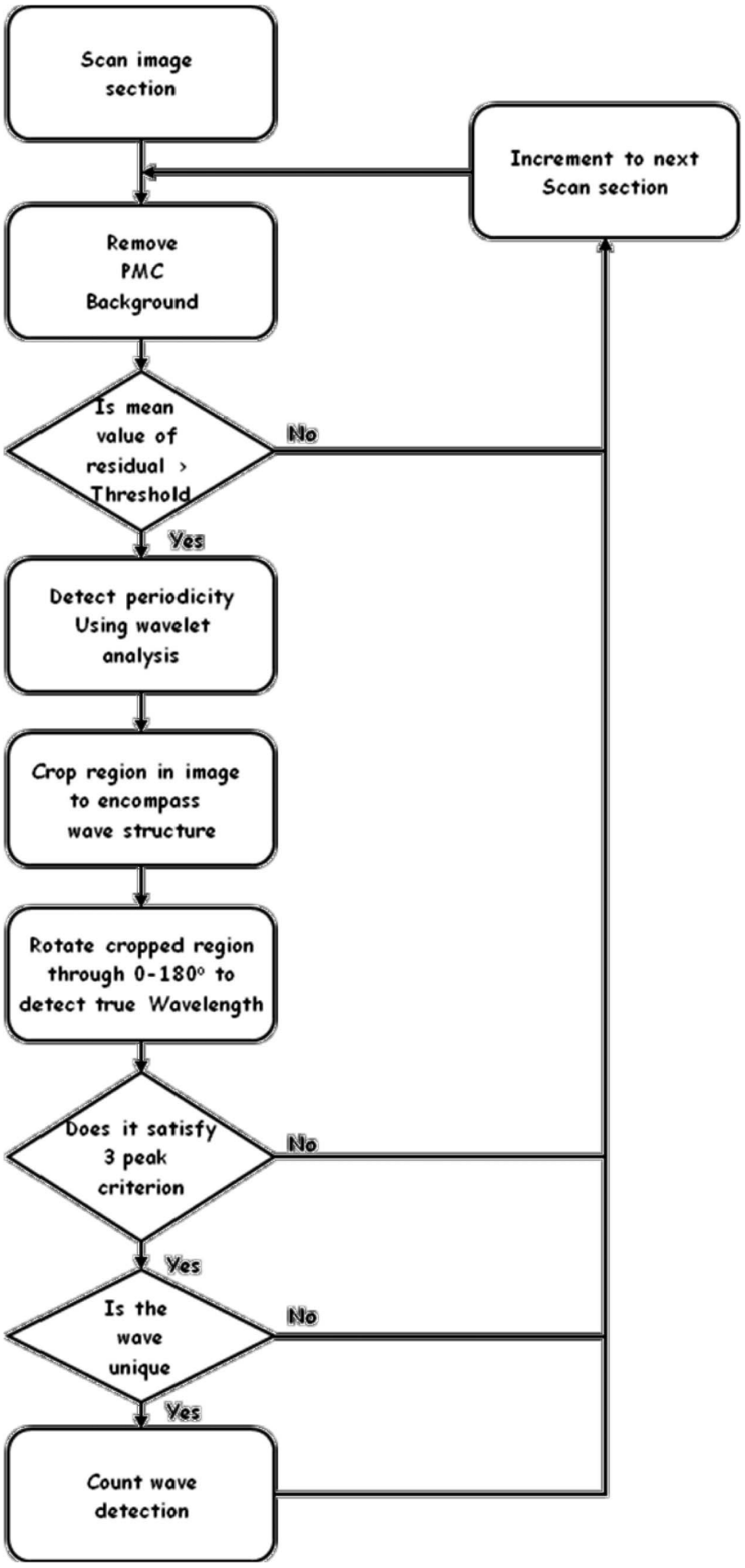

Figure 3. Graphical depiction of wave detection algorithm.

to these data from the trace 1 near the right edge of the CIPS image in Figure 1b. The residual, after subtraction of the polynomial fit, is then calculated. Through trial and error, we found that the strongest visually evident quasi monochromatic waves make perturbations in cloud albedo above 15×10^{-6} sr^{-1}, while perturbations less than 5×10^{-6} sr^{-1} are possibly camera artifacts, which includes pixel-to-pixel variations in the camera sensitivity and the associated variations in brightness across the surface of the image that might be detected as periodic structures. Hence for this analysis, results of AGW detections are for a threshold value of 10×10^{-6} sr^{-1} for the mean albedo value of the residual, while the error bars on the wave detections are for thresholds value ranging from 5×10^{-6} sr^{-1} to 15×10^{-6} sr^{-1}. Our threshold for wave detection is conservative, since the CIPS detection threshold for PMC is $\sim 1 \times 10^{-6}$ sr^{-1} [*Bailey et al.*, 2009; *Rusch et al.*, 2009; *McClintock et al.*, 2009].

[13] A wavelet analysis [*Torrence and Compo*, 1998] is then performed on the residual to determine the horizontal wavelength of any existing PMC structure. The wavelet transform can analyze time series that contain many different frequencies, or in the case of a spatial scan, with many composite wavelengths, and is well suited to the analysis of finite "wave packets" [*Rodenas and Garello*, 1998]. Compared to the Fourier transform, the wavelet method is more suitable for analysis of CIPS images that often show multiple wave structures. Because we are primarily interested in the wavelet power criteria, the choice of a "mother wavelet" is not critical and a Morlet wavelet was chosen [*Torrence and Compo*, 1998]. The wavelet analysis computes the mean power spectrum for the residual, and if a peak in the wavelet power spectrum is significantly above the power levels of a nonperiodic signal, then it is assumed to be a true feature. We have used a significance level of 95% for our analysis that implies that the peaks have 5% probability of being caused by noise in the data. The 95% confidence level has been computed by multiplying the mean power spectrum of the series by the 95th percentile value for chi-square, distributed with two degrees of freedom denoted by χ_2^2 [*Jenkins and Watts*, 1968; *Gilman et al.*, 1963]. The analysis presented in this paper considers peaks in the power spectrum lying outside of the so-called cone of influence, which is a region of the wavelet power spectrum where spurious peaks may be generated by the wavelet as a result of it introducing zeroes at the beginning and end of the data series to make it cyclic [*Torrence and Compo*, 1998].

[14] Once a coherent periodicity has been detected, the image is then cropped to include only the part of the image containing the detected wave field. The cropping makes a section of the image, that has dimensions of twice the detected wavelength from the center point of the detected structure in both directions along the column and 5 pixels (25 km), wide in the other dimension and also helps to reduce computing time. The cropped image is rotated through angles from 0° to 180° to determine the orientation and true horizontal wavelength of the wave structure. The wavelet will show maximum power when the wavefront is orthogonal to the trace under analysis [*Chandler*, 2005]. The cropping of the image to 5 pixels in the dimension across the trace limits the angles to which waves can be detected for larger-scale waves. Since that limitation can lead to a varying sensitivity with orientation for detection of longer wavelength waves, we make the assumption that AGWs are distributed isotropically and do not have any preferential orientations. A study on the orientations of the detected wave structures is in progress where this limitation in detecting true wave orientation will be addressed.

[15] For the purpose of this analysis, periodic structures are defined as a coherent set of at least three separated spatially extensive (3 pixels or 15 km wide), linear crests in the CIPS PMC images. The periodic structures have to satisfy this condition to be "detected. " In many CIPS images, the wave fields are seen extending over a large part of the image. In such cases, scans through the image will result in multiple detections of the same periodic structure. To eliminate this, the periodic structures also have to satisfy a uniqueness condition by which they have to be different from any previously detected structure in the image, by at least 10% of their wavelength. When two or more waves are detected in the same image with wavelengths within 10% of each other, the algorithm will always retain the first detected wave structure.

[16] Figure 2 is a four-panel plot of the wavelet power spectrum of the residual along the four traces marked in Figure 1b. Figure 2a is a plot of the power spectrum along trace 1. This trace is of sufficient length to include the large-scale structures, and the power spectrum clearly indicates a wave packet the dominant horizontal wavelength of which is 255 km. In Figure 2b, along trace 2, the presence of multiple waves with horizontal wavelengths centered around 150 km and 60 km can be seen in the wavelet power spectrum. The wave detection algorithm will cycle through the peak powers and crop the image to isolate these separate wave events as described above. Traces 3 and 4 in Figure 1b are representative of the cropping, and the wavelet power spectrum of these shortened scans are shown in Figures 2c and 2d which clearly show structures with horizontal wavelength distributions centered at 60 and 158 km in Figure 2c and 57 km in Figure 2d. The automated wave searching routine has a higher sensitivity for wave detection than the visual detection scheme presented by *Chandran et al.* [2009]. Visual analysis of CIPS images is biased toward the smaller-scale structures. This is because CIPS images provide a "top-down" integrated view of the PMC layer, and very often, the presence of multiple clouds across the image obscures the visual detection of larger-scale wave structures, which are spread over a larger region in the image. The visual analysis is biased toward picking wave events in individual clouds, and very often, the larger-scale structures will be missed. The method presented here represents a significant improvement over our earlier study.

3.1. Limitations of the Analysis

[17] In this section we discuss the limitations present in the wave detection scheme. Since the analysis was carried out on single camera images, the horizontal wavelength scales that can be detected are limited from 10 to 300 km. The size of the camera image thus limits the horizontal scale of wave structures that can be detected uniformly throughout the camera. The uniqueness condition discussed in section 3 results in undersampling of wave structures. False detections can occur from harmonics of the original wavelengths in the detection algorithm. Each of these limitations are discussed in detail in the following paragraphs. The limitations presented here do

not have any significant effect on the longitudinal variability of the derived wave structure.

[18] The horizontal scales of the detected wave structures vary from 10 to 300 km. Because of the three peak (trough) criteria for wave detection, only the shorter wavelengths (<165 km) can be detected uniformly in all parts of the camera. Above 165 km, the ability to detect wave structures in all parts of the camera progressively decreases with increasing wavelength, and at the upper limit of 300 km, wave structures can only be detected in ~55% of the camera, along the center, and at the edges. The results from the analysis of wave structures in section 4 are thus presented in two parts for wave structures <150 km and for all wave structures detected. The uniqueness condition that requires each detected wave to be at least 10% different in wavelength from all other waves detected in a particular image causes some wave structures to be missed. However, this should affect all the horizontal scales equally and not affect the longitudinal variability or distribution of horizontal wavelengths. Simulated studies of wave detections using the detection scheme have also shown that occasionally false wave detections occur at harmonics of ~50% and ~25% of the original wavelengths. We estimate that ~8% to 10% of the total number of wave detections is likely to be caused by such false detections. PMC layers are generally not horizontal and often display a tilt. Lidar soundings of NLC [e.g., *Baumgarten and Fiedler*, 2008; *Schöch*, 2007] have shown descending NLC layers with time. The maximum observed descent rates of <100 cm/s [*Thayer et al.*, 2003], possibly caused by wave-related vertical winds, correspond to maximum layer tilts <6° assuming drift speeds of 10 m/s at the lidar site. Periodically tilted structures of otherwise homogeneous clouds will cause wavelike cloud albedo perturbations above our detection thresholds and enhance the detection of short wavelength waves that probably have higher maximum tilt angles. These geometric effects can potentially enhance the detection probability of the smaller wavelengths.

3.2. Normalization and Selection of Analysis Region

[19] *Olivero and Thomas* [1986] and *Merkel et al.* [2008] have shown that regions of high PMC brightness coincide with regions of high PMC occurrences. The CIPS AGW detections depend on PMC occurrence as well as brightness. *Merkel et al.* [2008] have shown that the PMC occurrence frequency as well as SABER measured temperatures at 83 km has a longitudinal variability which is reproduced as overplots along with the AGW longitudinal variability in Figure 7. If the AGW activity was zonally symmetric (no variation with longitude), the AGW structure observed by CIPS in longitude is expected to be directly correlated with PMC longitudinal structure. This is due to the fact that CIPS can only measure AGWs when PMCs are present. To estimate the impact of this observational bias, we have normalized the CIPS-measured relative AGW occurrence frequency (WOF) by an estimate of the relative PMC occurrence frequency (COF). A weighting factor, which estimates the percentage of time that a PMC is present at a given location, was derived from the COF. The COF is a level 4 CIPS data product derived from all four cameras and not just the most sunward viewing camera that was used for our AGW analysis. However, the COF is primarily driven by cloud detections from the forward viewing camera because of ice scattering properties and the CIPS viewing geometry. The normalization can be explained using the following equation:

$$\mathrm{NWOF}(\varphi) = \frac{\left(\frac{\mathrm{WOF}(\varphi)}{\mathrm{COF}(\varphi)}\right)}{\min\left(\frac{\mathrm{WOF}(\varphi)}{\mathrm{COF}(\varphi)}\right)}, \quad (1)$$

where φ is the longitude. After normalization of the AGW occurrence frequency (NWOF), the observed longitudinal variability becomes more pronounced than in the unnormalized case (see Figure 5), indicating that this longitudinal variability is a robust feature in the observations and is not the result of a systematic variation in the occurrence of clouds.

[20] *Garcia* [1989] and more recently *Chu et al.* [2009] have postulated that at temperatures well below the frost point, AGW does not cause sufficient temperature change to significantly affect mean cloud brightness. However, for temperatures near the frost point, the warmer regions of AGW can destroy the ice and hence significantly affect the mean brightness. Chu's postulate was developed to explain the lack of a negative correlation of stratospheric PMC occurrence rates with AGW activity at the South Pole, while the presence of negative correlations were observed at Rothera (67.5°S). In our study we restrict our analysis to the latitude band between 70° and 80°, so that the range of temperatures, measured by SABER, is only about 2 K about the mean temperature of ~138 K, which is well below the frost point. We have performed a series of 2-D CARMA modeling studies (which will be described in a forthcoming publication) that show that at these mean temperatures, the small changes in temperature (~2 K) do not significantly affect the overall cloud albedo or produce significant variations in albedo perturbations because of AGW. Hence, the observed variations in local temperature do not influence our ability to detect AGW.

[21] At the higher latitudes where the longitudes are spatially closer, a detected wave will likely extend over multiple longitudes effectively masking longitudinal variations. Equatorward of 65° in both hemispheres, the PMC occurrences are fewer in number, and the data do not provide sufficient statistics to perform a longitudinal variability study. Hence, the longitudinal analysis presented in this paper is limited to latitudes between 70° and 80°.

4. Results

[22] In this section we present details of the longitudinal variability as well as a distribution of horizontal scales in periodic structures detected in PMC in the 2007 and 2008 Northern Hemisphere (NH) and 2007–2008 and 2008–2009 Southern Hemisphere (SH) summer seasons. The NH PMC season runs from the last week of May to late August while the SH PMC season runs from December through the middle of March.

[23] Figure 4 shows the distribution of the horizontal wavelengths for PMC structures detected in the four seasons. In the two NH seasons and the 2008–2009 SH season, 1125 orbits were analyzed, while for the 2007–2008 SH season, 650 orbits were analyzed. The fewer number of orbits in the 2007–2008 SH was due to a one-time operational issue with the satellite, resulting in data loss near season's end.

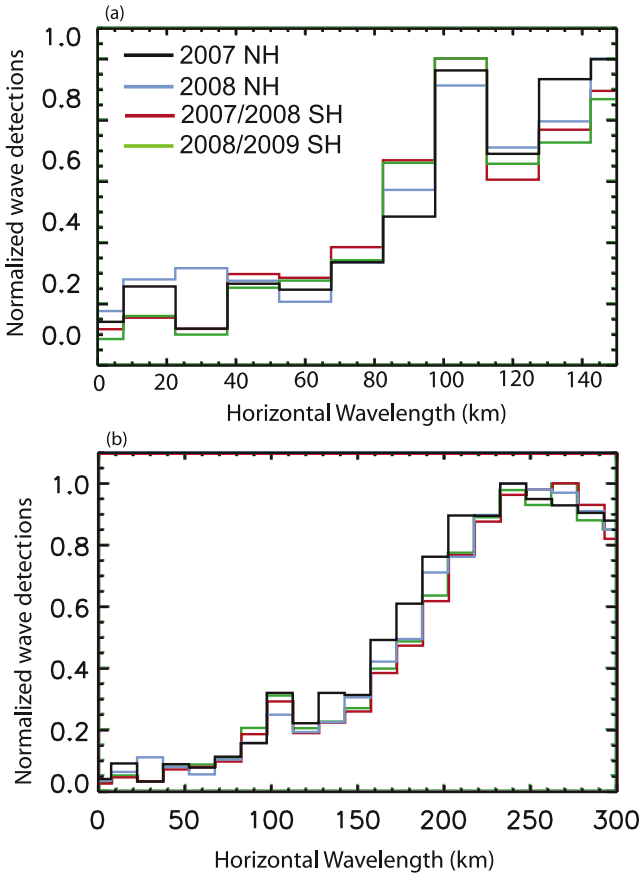

Figure 4. Histogram plot showing distribution of horizontal scales of structures detected in PMC (a) for wave structures less than 150 km in horizontal scales and (b) for all detected wave structures.

Figure 4a shows the distribution of structures with horizontal scales less than 150 km that can be detected uniformly throughout the entire camera. Figure 4b shows the distribution of the entire spectrum of PMC-detected structures. As can be seen in Figure 4b, in all the seasons, there are more larger-scale waves than shorter-scale waves. In both hemispheres, the distributions of horizontal wavelengths show a peak at ~250 to 300 km, close to the largest resolvable horizontal wavelength from our analysis. The number of wave events detected per orbit is approximately the same (~11/orbit) in the 2007 NH season and both the SH seasons, while the 2008 NH season is slightly higher (~12/orbit). It should be noted that in the SH generally there are less PMC compared to the NH, and hence, the number of waves detected per PMC is higher in the SH than in the NH.

[24] To investigate the longitudinal variability in wave occurrence, the WOF for the latitude band between 70° and 80° in both hemispheres is plotted in 15° longitude bins and compared with similar cloud occurrence frequency plots from CIPS and deviations from SABER-measured mean temperatures at 83 km derived from an analysis done by *Merkel et al.* [2009]. The mean SABER temperatures were ~138 K for the 2007 and 2008 NH seasons, while the SH was significantly warmer at 145 K for the 2007–2008 and 2008–2009 SH seasons. To make this comparison, data from summer solstice to 25 days after solstice for the NH and 10 days before and after solstice (a total of 20 days) for the SH were averaged in specific longitude bins. The choice of 20 days (from 10 days before solstice to 10 days after solstice) in the SH was because we did not have continuous coverage in SABER data for the required 25 days after solstice. *Merkel et al.* [2009] have shown that planetary wave signatures are seen in temperature as well as PMC albedo (frequency). The choice of the 25 and 20 day periods minimizes the effects from planetary wave activity and any short-term (day-to-day) influences.

[25] Figures 5, 6, and 7 are four-panel plots illustrating the longitudinal variability in the observed PMC structures for all detected wave structures (WOF), wavelengths less than 150 km, and for all detected wave structures normalized by COF (NWOF), respectively. Figures 5–7 (a–d) are for the 2007 NH, 2008 NH, 2007–2008 SH, and 2008–2009 SH PMC seasons, respectively. The WOF have been normalized, so that a value of one corresponds to the longitude bin with lowest wave activity. As discussed earlier, the WOF values are plotted for a detection threshold of 10×10^{-6} sr^{-1}, while the error bars in the plots are the standard deviation of wave occurrence frequencies derived from using different detection thresholds ranging from 5×10^{-6} sr^{-1} to 15×10^{-6} sr^{-1}. As can be seen from the plots, changing the threshold values does not appreciably affect the longitudinal variability present in the detected structures. The wave structure occurrence observed in CIPS data shows a negative correlation with CIPS-observed PMC occurrence and a positive correlation with SABER-measured temperatures at 83 km. Table 1 lists the correlation of the CIPS-observed wave structures with PMC occurrences and SABER temperatures. The correlation coefficients have been calculated as the ratio of the covariance of the COF and AGW occurrences to the product of their standard deviations, and values above 0.5 indicate significant correlations at 95% confidence levels. In all the four seasons, the AGW occurrence frequency and PMC occurrence frequency show significant anticorrelations. For the 2007 NH and 2007–2008 SH seasons, the AGW occurrences are correlated with SABER temperatures, while in the 2008 NH and 2008–2009 SH seasons, there does not appear to be a significant correlation. As stated in section 3, since the AGW detections depend on PMC occurrence, the AGW occurrence was expected (if there were no longitudinal variation in AGW activity) to be correlated with PMC occurrence, and hence, normalizing the AGW occurrence frequency with PMC occurrence frequency should have resulted in a straight line in the absence of any zonal variation in AGW activity. However, Figure 5 shows that there is a clear longitudinal variation in AGW activity even without normalizing the WOF with the COF. Column 1 in Table 1 lists the correlation coefficients of the unnormalized WOF with PMC occurrence and SABER temperatures for all four seasons, while column 2 lists the corresponding correlation coefficients for the NWOF. Normalizing the WOF with COF does not change the correlation coefficients appreciably (<0.1) except for the 2008 NH season. The longitudinal variability is a stationary feature that does not change character with time during the period of analysis.

[26] From the four seasons of PMC data analyzed, it can be observed that there are regions of high and low wave activity in both hemispheres. In the 2007 and 2008 NH and the 2008–2009 SH seasons, the magnitude of variation in AGW activity detected in PMC vary by as much as 30% between the region

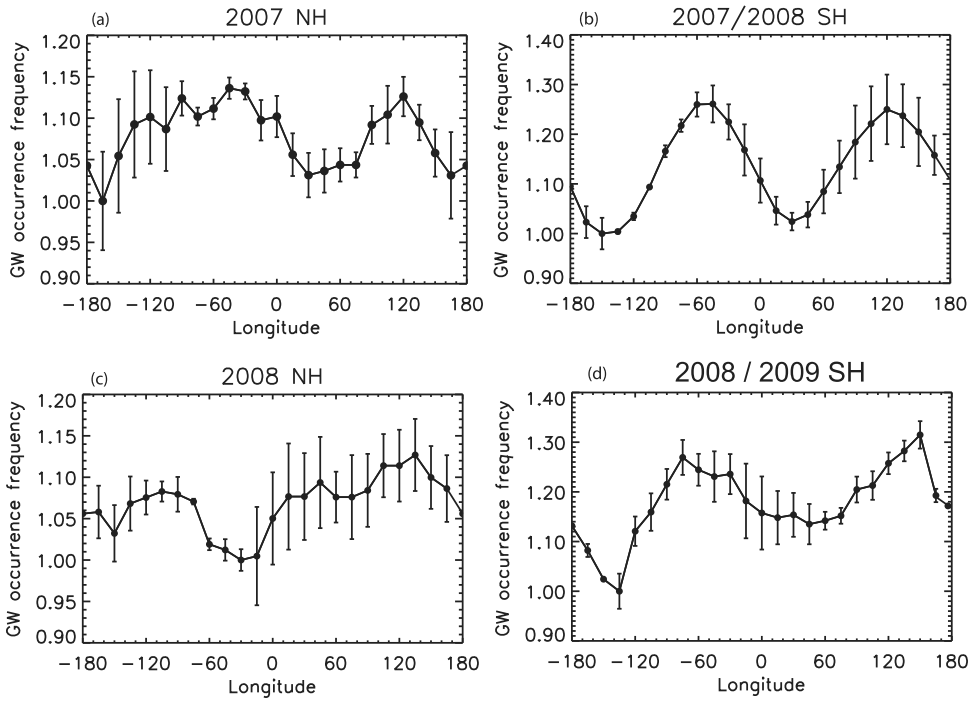

Figure 5. Longitudinal variability in the relative AGW occurrence (WOF). (a) 2007 NH, (b) 2008 NH, (c) 2007-2008 SH, and (d) 2008–2009 seasons.

with highest and lowest wave activity. In the 2007–2008 SH season, the magnitude of variation in wave activity between low and high wave activity regions is as much as 140%. Between the 2007 and 2008 NH PMC seasons, while there is a change in the structure of the longitudinal variability in the observed PMC structures, the regions of lowest wave activity and highest PMC occurrence remains the same (north of continental Asia between 60° and 120° East). While the

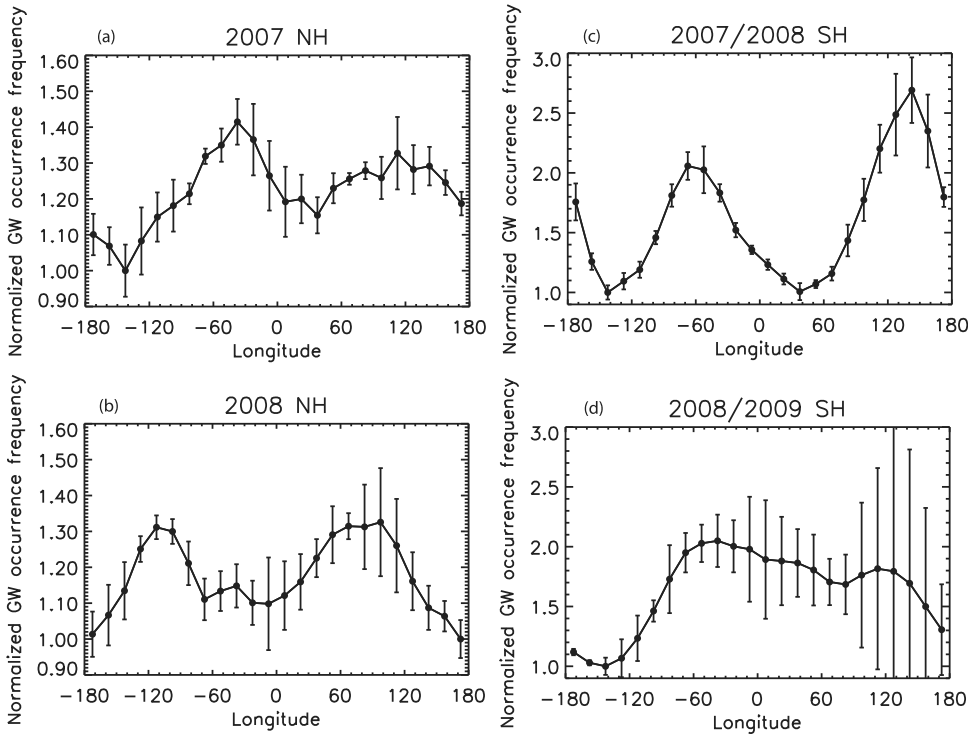

Figure 6. Longitudinal variability in the normalized AGW occurrence (NWOF) for structures less than 150 km in horizontal scales for (a) 2007 NH, (b) 2008 NH, (c) 2007–2008 SH, and (d) 2008–2009 seasons.

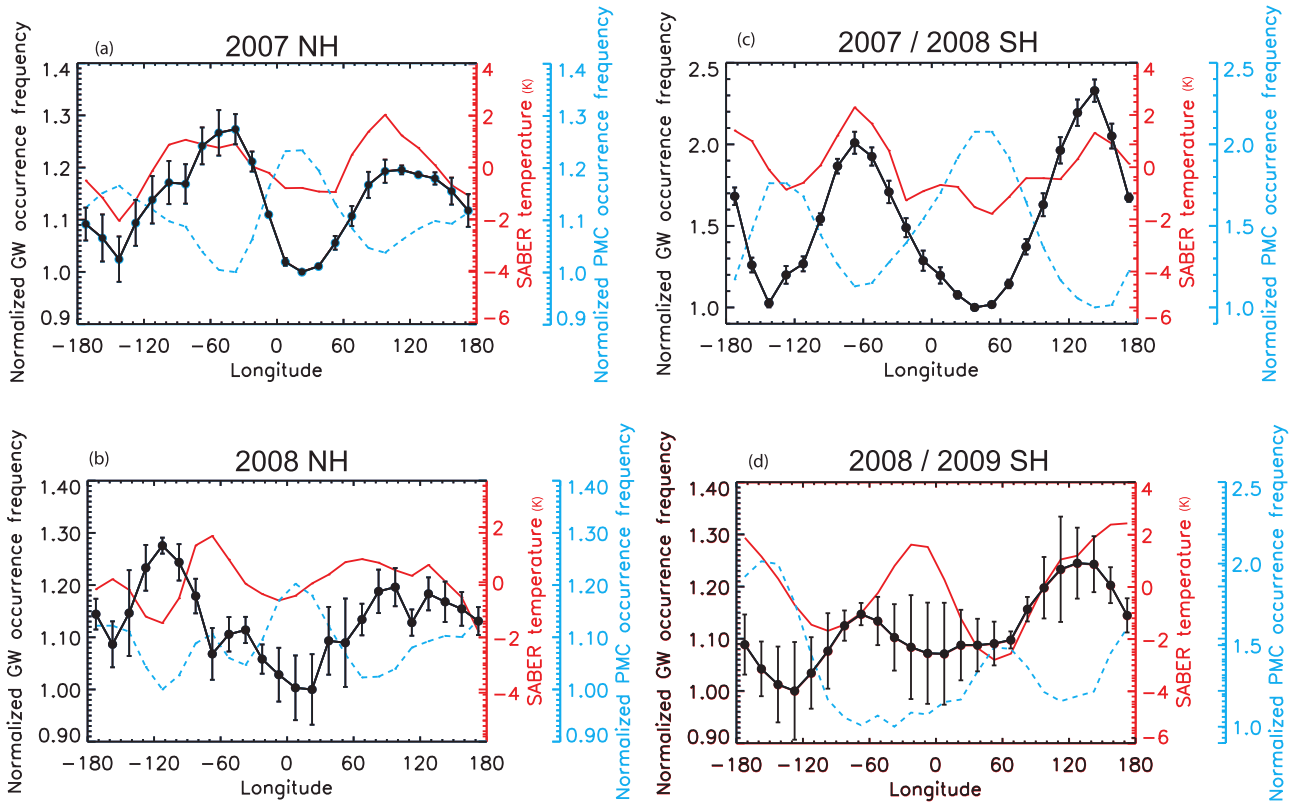

Figure 7. Longitudinal variability in the normalized AGW occurrence (NWOF), SABER temperature data (red line), and CIPS-observed normalized cloud occurrence (COF) (dashed blue lines) for (a) 2007 NH, (b) 2008 NH, (c) 2007–2008 SH, and (d) 2008–2009 seasons.

longitudinal structure remains the same in the Eastern Hemisphere, the Western Hemisphere shows significant differences between the two seasons. Regions such as Western Greenland and Canada (50°W–120°W), North of Central Russia (60°E–90°E) over the Ural mountains, and south of the Antarctic Peninsula (30°W–90°W) appear as regions of high AGW activity.

5. Discussion and Conclusions

5.1. Influence of Tides on Observations

[27] The AIM spacecraft is in a Sun-synchronous orbit thus only making measurements at two local times each day. As is the case for any discretely sampled time series, oscillations present at periods less than half the sampling period will be aliased in the spectrum. Because satellites sample in a coupled time-longitude frame, the aliasing relation is also coupled in frequency and wave number. Details of the underlying aliasing theory for Sun-synchronous satellites are given by *Salby* [1982a, 1982b]. *Forbes et al.* [2008] have shown that atmospheric tides, which are global scale oscillations with periods that are a harmonic of a solar day, can be expressed as $A_{n,s}\cos(n\Omega t_{LT} + (s-n)\lambda - \phi_{n,s}$, where A and ϕ are the wave amplitude and phase, Ω is the rotational rate of the Earth (2π day^{-1}), t_{LT} is local time (days), λ is longitude (radians), s is the zonal wave number (0, 1, 2, 3, …), and n is the solar harmonic index (±1, ±2, ±3, …), where the sign indicates the direction of propagation (positive westward). For example, $n = +1$ indicates the diurnal tide with a period of 24 h while $n = +2$ indicates the semidiurnal tide with a period of 12 h and so forth. By definition, the migrating tides are fixed in local time such that $s = n$. For example, $s = n = 1$ is the migrating diurnal tide and $s = n = 2$ is the migrating semidiurnal tide. For a Sun-synchronous satellite, sampling at a single local time, an ambiguity between time and longitude arises, thus, giving rise to the aliasing effect mentioned above.

Table 1. Correlation of AGW Occurrences With SABER Temperatures and PMC Occurrences[a]

	Unnormalized WOF (All Wavelengths)		NWOF (All Wavelengths)		NWOF (l_n < 150 km)	
Season	CIPS PMC Occurrence	SABER Temperature	CIPS PMC Occurrence	SABER Temperature	CIPS PMC Occurrence	SABER Temperature
2007 NH	**−0.74**	**0.61**	**−0.82**	**0.6**	**−0.71**	**0.52**
2008 NH	**−0.55**	0.21	**−0.78**	0.33	−0.61	0.27
2007–2008 SH	**−0.89**	**0.73**	**−0.94**	**0.72**	**−0.87**	**0.68**
2008–2009 SH	**−0.86**	0.38	**−0.92**	0.4	**−0.84**	0.36

[a]Correlation values that are significant at 95% confidence levels are in bold.

As a result, waves that are constant cannot be distinguished and are aliased. Consider the migrating tides where $s = n$ thus $k = 0$ imply that using data from a Sun-synchronous satellite which samples at a single local time, the effects of the migrating tides cannot be resolved, and in fact, these components alias to the zonal mean ($s = n = 0$). With observations from two local times, the alias impact can be reduced.

[28] While we are not concerned with the impact of the migrating tides, here we are concerned with the nonmigrating tides ($s \neq n = 1, 2, \ldots$), which alias in a similar way to stationary planetary waves. Stationary planetary waves have no temporal variation ($n = 0$) but have longitudinal variation ($s = 1, 2, \ldots$), such as shown in the zonal structure observed in the CIPS and SABER data presented herein. A zonal wave 2 stationary planetary wave will have $k = 2$ as will the nonmigrating diurnal tide ($n = 1$) with zonal wave numbers $s = 3$ or -1 and the nonmigrating semidiurnal tide ($n = 2$) zonal wave numbers $s = 0$ or 4. Satellite [*Zhang et al.*, 2006] and model [*Hagan and Forbes*, 2002, 2003] results indicate that the westward propagating $s = 3$ (W3) and eastward propagating $s = 2$ (E2) nonmigrating diurnal tidal components are not effectively excited in the atmosphere. Additionally, using a network of ground-based radars in the Antarctic, *Murphy et al.* [2006] did not observe any significant nonmigrating diurnal tidal components indicating that the likelihood is small that these components could be aliased in the results presented here.

[29] It is known that a large nonmigrating $s = -1$ (W1) semidiurnal tide exists during the summer in the Antarctic mesosphere and lower thermosphere [*Hernandez et al.*, 1993; *Portnyagin et al.*, 1998]. Additionally, *Murphy et al.* [2006] have shown the existence of a zonally symmetric $s = 0$ semidiurnal tide in the horizontal wind field present in the summer middle atmosphere above Antarctica. Recently, *Iimura et al.* [2009] produced a climatology of the nonmigrating tides in the meridional wind field over Antarctica which shows the presence of a strong W1 component and weaker S0 component but no significant W4 component.

[30] Of the four possible nonmigrating tidal components that could be aliased in the CIPS data, only one, the S0 nonmigrating semidiurnal tide, has been shown to exists at high latitudes. Because the TIMED satellite is not Sun-synchronous which implies precession over local time and the data presented were analyzed over a 30 day interval, the potential of S0 nonmigrating semidiurnal tide aliasing into the SABER results is low. However, since little is known about the latitudinal structure of the $s = 0$ nonmigrating semidiurnal tide in temperature, we cannot discount the possibility that this component impacts the 30 day averaged SABER results.

[31] The influence of the S0 nonmigrating semidiurnal tide must also be considered in the interpretation of the CIPS AGW results. The longitudinal variability in the gravity waves observed by CIPS could be due to variations in the source region or variations in the intervening wind field, thus, selectively filtering and eliminating some portion of the gravity wave spectrum. If one consider the possibility of filtering, an $s = 2$ longitude structure could be due to a stationary planetary wave pattern present in the wind field or a nonmigrating semidiurnal S0 structure as the resulting $s = 2$ structure would appear the same from a Sun-synchronous satellite. Since stationary planetary wave activity is typically minimum during the summer months [*Smith*, 1983, 1997], the S0 nonmigrating semidiurnal tide could be playing the more important role in the observed gravity wave structure. At this point, more work is necessary to understand the extent to which tides may influence our results. This work is underway but is beyond the scope of this paper. For now, we assume there is no influence of tides on our results.

5.2. Summary of Results

[32] The most significant result from our analysis is the presence of a longitudinal variability in PMC wave structures as well as PMC occurrence and temperature. The longitudinal variability in PMC wave structures is anticorrelated with the PMC variability, while deviations in SABER temperatures from mean temperatures at 83 km is correlated with AGW occurrences in two out of the four seasons. Large heating or cooling rates in the middle atmosphere, possibly related to dissipation of AGW, were found in observations by *Tao and Gardner* [1995] and *Meriwether et al.* [1998]. *Walterscheid* [1981a] and *Liu* [2000] have shown that AGW breaking in the lower thermosphere may produce a downward heat flux, which cools the mesopause region and heats the region immediately below. An inspection of SABER temperature structure at different altitudes indicates that the warmer regions at PMC altitudes have colder regions above, and at other times vice versa. On the basis of these results, we suggest that dissipating AGW are heating the atmosphere at PMC altitudes, either adiabatically during their propagation or by driving a downward heat flux from the altitudes at which they break, which in turn heats the atmosphere, causing ice sublimation and hence fewer and dimmer PMC.

[33] In both hemispheres, the distributions of horizontal wavelengths show a peak at ~250 to 300 km, close to the largest resolvable horizontal wavelength from our analysis. *Carbary et al.* [2000], using data from the ultraviolet and visible imaging and spectrographic imaging instrument on the Midcourse Space Experiment satellite, observed PMC horizontal structures along the subsatellite track, ranging from 100 to 3000 km with a peak at ~300 to 400 km. The PMC occurrence frequency and brightness measured from the OSIRIS instrument on board the Odin satellite have shown similar longitudinal patterns in PMC occurrences with low PMC occurrence and brightness being observed consistently between 70°W and 120°W in the SH over the Antarctic peninsula and between 50°E and 130°E in the NH [*Petelina and Rusch*, 2008].

[34] [*Gerrard et al.*, 2004] used a ray tracing model to show that the AGW observed over Söndrestrom were most likely generated from convective sources over Baffin Bay, west of Greenland. It is possible that the waves observed in PMC images are generated from convective sources or from geostrophic adjustments and propagate to the regions where they are observed. However, the regions of high AGW activity described in section 4 suggest that these AGW could be orographic in origin. Since orographically generated AGW (mountain waves) have phase speeds close to zero, they are expected to propagate to mesospheric heights only during the winter months when the zero wind line (a critical level for mountain waves) lies above 90 km [*Eckermann*, 1995]. *Fritts et al.* [2009] have shown that secondary waves may be generated from wave-wave interactions and wave breaking. Secondary waves generated from mountain waves breaking

at critical levels below 83 km could propagate to PMC altitudes and account for wave activity over orographic sources. A recent study [K. Nielsen, Naval Research Laboratory, personal communication, 2009] using NOGAPS-ALPHA model show that the meridional and zonal wind structure in summer could allow "clear channels" to exist, which would allow mountain waves (with zero phase speeds) to propagate to mesospheric altitudes even in summer.

[35] Our observations support the theory postulated by *Gerrard et al.* [2002] and indicated by *Turco et al.* [1982], *Jensen and Thomas* [1994], and *Rapp et al.* [2002] that while on monthly time scales, AGW drive the refrigeration process that produces the cold summer mesopause and, hence, cloud formation. These waves tend to destroy PMC on shorter daily scales and within specific geographic regions. The results from lidar observations made at different locations have been inconclusive regarding correlations between PMC backscatter and local AGW activity. Lidar measurements made at Söndrestrom (67°N, 51°W), Greenland, and at Rothera (67.5°S, 68°W), Antarctica, which have showed AGW activity to be inversely proportional to PMC backscattering, lie in regions where AGW activity is generally higher in both hemispheres. Kuhlungsborn (54°N, 11.7°E), Germany; Alomar (69.3°N, 17.6°W), Norway; and Davis (68.6°S, 78°E), Antarctica, where lidar observations noted no significant correlation between PMC brightness and stratospheric AGW activity, lie in regions of low AGW activity as seen from CIPS observations. Hence, our analysis suggests that the apparently conflicting results between fixed lidar sites may result from the local differences in the existing background temperatures at PMC altitudes and the amount of local AGW activity. In this context, CIPS observations provide a unique opportunity to study the longitudinal differences in AGW activity and its effects on PMC occurrence.

[36] Current and future work include a detailed study of LT and tidal effects as potential causes for the observed longitudinal variability, a detailed comparison between OSIRIS and CIPS PMC longitudinal structures, a study of the orientations of the detected wave structures, and an investigation of the propagation of mountain waves to mesospheric altitudes in summer to account for a possible orographic origin of some of the observed PMC wave structures.

[37] **Acknowledgments.** AIM was developed as part of the NASA Small Explorer series of missions under contract NAS5-03132. We acknowledge the efforts of the entire development, engineering, science, and operations teams. The authors would also like to acknowledge the discussions and contributions from Kim Nielsen, Eric Jensen, Svetlana Petelina, and Chris Jeppesen for their help with science inputs and in analyzing the data. We would also like to acknowledge the anonymous reviewers for their constructive comments in improving the manuscript.

References

Bailey, M. S., G. E. Thomas, D. W. Rusch, A. W. Merkel, C. Jeppesen, J. N. Carstens, C. E. Randall, W. E. McClintock, and J. M. Russell III (2009), Phase functions of polar mesospheric cloud ice as observed by the CIPS instrument on the AIM Satellite, *J. Atmos. Sol.-Terr. Phys.*, *71*, 373–380, doi:10.1016.j.jastp.2008.10.011.

Baumgarten, G., and J. Fiedler (2008), Vertical structure of particle properties and water content in noctilucent clouds, *Geophys. Res. Lett.*, *35*, L10811, doi:10.1029/2007GL033084.

Carbary, J. F., D. Morrison, and G. J. Romick (2000), Transpolar structure of polar mesospheric clouds, *J. Geophys. Res.*, *105*, 24,763–24,769.

Chandler, R. C. (2005), A wavelet based method for the extraction of sea wave orientation, paper presented at OCEANS 2005 MTS/IEEE meeting, Washington, D.C., Sep. (050214-10).

Chandran, A., D. W. Rusch, S. E. Palo, G. E. Thomas, and M. J. Taylor (2009), Gravity wave observations in the summertime polar mesosphere from the cloud imaging and particle size (CIPS) experiment on the AIM Spacecraft, *J. Atmos. Sol.-Terr. Phys.*, *71*, 392–400, doi:10.1016/j.jastp.2008.09.041.

Chu, X., C. Yamashita, P. J. Espy, G. J. Nott, E. J. Jensen, H.-L. Liu, W. Huang, and J. P. Thayer (2009), Responses of polar mesospheric cloud brightness to stratospheric gravity waves at the South Pole and Rothera, Antarctica, *J. Atmos. Sol.-Terr. Phys.*, *71*, 434–445, doi:10.1016/j.jastp.2008.10.002.

Eckermann, S. D. (1995), Effect of background winds on vertical wave number spectra of atmospheric gravity waves, *J. Geophys. Res.*, *100*(D7), 14,097–14,112.

Forbes, J. M., X. Zhang, S. Palo, J. Russell, C. J. Mertens, and M. Mlynczak (2008), Tidal variability in the ionospheric dynamo region, *J. Geophys. Res.*, *113*, A02310, doi:10.1029/2007JA012737.

Fritts, D. C., J. R. Isler, and G. E. Thomas (1993), Wave breaking signatures in noctilucent clouds, *Geophys. Res. Lett.*, *20*(19), 2039–2042.

Fritts, D. C., L. Wang, J. Werne, T. Lund, and K. Wan (2009), Gravity wave instability dynamics at high Reynolds numbers. Part I: Wave field evolution at large amplitudes and high frequencies, *J. Atmos. Sci.*, *66*, 1126–1148, doi:10.1175/2008JAS2726.1.

Gadsden, M., and P. Parviainen (1995), Observing noctilucent clouds, *International Association of Geomagnetism and Aeronomy*. ISBN 0-9650686-0-9 (Available online at http://www.iugg.org/IAGA/iaga_pages/pdf/ONC_Sep06.pdf).

Garcia, R. R. (1989), Dynamics, radiation, and photochemistry in the mesosphere: Implications for the formation of noctilucent clouds, *J. Geophys. Res.*, *94*(D12), 14,605–14,615.

Gerding, M., J. Höffner, M. Rauthe, W. Singer, M. Zecha, and F.-J. Lübken (2007), Simultaneous observation of noctilucent clouds, mesospheric summer echoes, and temperature at a midlatitude station (54°N), *J. Geophys. Res.*, *112*, D12111, doi:10.1029/2006JD008135.

Gerrard, A. J., T. J. Kane, and J. P. Thayer (1998), Noctilucent clouds and wave dynamics: Observations at Sondrestrom, Greenland, *Geophys. Res. Lett.*, *25*(15), 2817–2820.

Gerrard, A., J. Thayer, and T. Kane (2002), Mesospheric clouds and the duality of gravity waves, *Eos Trans. AGU*, *83*(43), doi:10.1029/2002EO000344.

Gerrard, A. J., T. J. Kane, S. D. Eckermann, and J. P. Thayer (2004), Gravity waves and mesospheric clouds in the summer middle atmosphere: A comparison of lidar measurements and ray modeling of gravity waves over Sondrestrom, Greenland, *J. Geophys. Res.*, *109*, D10103, doi:10.1029/2002JD002783.

Gilman, D. L., F. J. Fuglister, and J. M. Mitchell Jr. (1963), On the power spectrum of "red noise.", *J. Atmos. Sci.*, *20*, 2867–2878.

Hagan, M. E., and J. M. Forbes (2002), Migrating and nonmigrating diurnal tides in the middle and upper atmosphere excited by tropospheric latent heat release, *J. Geophys. Res.*, *107*(D24), 4754, doi:10.1029/2001JD001236.

Hagan, M. E., and J. M. Forbes (2003), Migrating and nonmigrating semidiurnal tides in the upper atmosphere excited by tropospheric latent heat release, *J. Geophys. Res.*, *108*(A2), 1062, doi:10.1029/2002JA009466.

Haurwitz, B., and B. Fogle (1969), Wave forms in noctilucent clouds, *Deep-Sea Res.*, *16*, 85–95.

Hernandez, G., G. J. Fraser, and R. W. Smith (1993), Mesospheric 12-h oscillation near South Pole, Antarctica, *Geophys. Res. Lett.*, *20*, 1787–1790.

Hecht, J. H., J. P. Thayer, D. J. Gutierrez, and D. L. Mckenzie (1997), Multi instrument zenith observations of Noctilucent clouds over Greenland on July 30/31, 1995, *J. Geophys. Res.*, *102*(D2), 1959–1970.

Hines, C. O. (1968), A possible source of waves in noctilucent clouds, *Space Res.*, *IX*, 170–174.

Holton, J. R. (1983), The influence of gravity wave breaking on the general circulation of the middle atmosphere, *J. Atmos. Sci.*, *40*, 2497–2507.

Iimura, H., S. E. Palo, Q. Wu, T. L. Killeen, S. C. Solomon, and W. R. Skinner (2009), Structure of the nonmigrating semidiurnal tide above Antarctica observed from the TIMED Doppler interferometer, *J. Geophys. Res.*, *114*, D11102, doi:10.1029/2008JD010608.

Innis, J., A. R. Klekociuk, R. J. Morris, A. Cunningham, A. Graham, and D. J. Murphy (2008), A study of the relationship between stratospheric gravity waves and polar mesospheric clouds at Davis, Antarctica, *J. Geophys. Res.*, *113*, D14102, doi:10.1029/2007JD009031.

Jenkins, G. M., and D. G. Watts (1968), *Spectral Analysis and Its Applications*, 525 pp., Holden-Day, San Francisco, Calif.

Jensen, E. J., and G. E. Thomas (1994), Numerical simulations of the effects of gravity waves on noctilucent clouds, *J. Geophys. Res.*, *99*(D2), 3421–3430.

Leovy, C. (1964), Simple models of thermally driven mesospheric circulation, *J. Atmos. Sci.*, *21*(3), pp. 238–248.

Liu, H.-L. (2000), Temperature changes due to gravity wave saturation, *J. Geophys. Res.*, *105*(D10), 12,329–12,336.

Lübken, F.-J. (1999), Thermal structure of the Arctic summer mesosphere, *J. Geophys. Res.*, *104*(D8), 9135–9149.

McClintock, W. E., D. W. Rusch, G. E. Thomas, A. W. Merkel, M. R. Lankton, V. A. Drake, M. S. Bailey, and J. M. Russell III (2009), The cloud imaging and particle size experiment on the Aeronomy of Ice in the Mesosphere mission: Instrument concept, design, calibration and on-orbit performance, *J. Atmos. Sol.-Terr. Phys.*, *71*(3–4), 340–355, doi:10.1016/j.jastp.2008.10.011.

Meriwether, J. W., X. Gao, V. B. Wickwar, T. Wilkerson, K. Beissner, S. Collins, and M. E. Hagan (1998), Observed coupling of the mesosphere inversion layer to the thermal tidal structure, *Geophys. Res. Lett.*, *25*, 1479–1482.

Merkel, A. W., D. W. Rusch, G. E. Thomas, S. E. Palo, S. M. Bailey, J. M. Russell, M. Hervig, and A. Chandran (2008), Longitudinal variability of polar mesospheric cloud (PMC) albedo and frequency from the cloud imaging and particle size experiment: Comparison of the 2007 and 2008 Northern Hemisphere cloud seasons, AGU Fall 2008 meeting, San Francisco, Calif., 15–19 December, SA43A-1563.

Merkel, A. W., D. W. Rusch, S. E. Palo, J. M. Russell III, and S. M. Bailey (2009), Mesospheric planetary wave effects on global PMC variability inferred from AIM-CIPS and TIMED-SABER for the northern summer 2007 PMC season, *J. Atmos. Sol.-Terr. Phys.*, *71*(3–4), 381–391, doi:10.1016/j.jastp.2008.12.001.

Murphy, D. J., et al. (2006), A climatology of tides in the Antarctic mesosphere and lower thermosphere, *J. Geophys. Res.*, *111*, D23104, doi:10.1029/2005JD006803.

Olivero, J. J., and G. E. Thomas (1986), Climatology of polar mesospheric clouds, *J. Geophys. Res.*, *43*(12), 1263–1274.

Petelina, S. V., and D. W. Rusch (2008), Detection of mesospheric gravity waves in Odin/OSIRIS PMC data in 2002–2008, AGU Fall 2008 meeting, SA43A-1566.

Portnyagin, Y. I., J. M. Forbes, N. A. Makarov, E. G. Merzlyakov, and S. Palo (1998), The summertime 12-h wind oscillation with zonal wave number $s = 1$ in the lower thermosphere over the South Pole, *Ann. Geophys.*, *16*, 828–837.

Rapp, M., F.-J. Lübken, A. Müllemann, G. E. Thomas, and E. J. Jensen (2002), Small-scale temperature variations in the vicinity of NLC: Experimental and model results, *J. Geophys. Res.*, *107*(D19), 4392, doi:10.1029/2001JD001241.

Rapp, M., and G. E. Thomas (2006), Modeling the microphysics of mesospheric ice particles: assessment of current capabilities and basic sensitivities, *J. Atmos. Sol.-Terr. Phys.*, *68*, 715–744, doi:10.1016/j.jastp.2005.10.015

Remsberg, E. E., et al. (2008), Assessment of the quality of the Version 1.07 temperature versus pressure profiles of the middle atmosphere from TIMED/SABER, *J. Geophys. Res.*, *113*, D17101, doi:10.1029/2008JD010013.

Rodenas, J. A., and R. Garello (1998), Internal wave detection and location in SAR images using wavelet transform, *IEEE Trans. Geosci. Remote Sens.*, *36*(5), 1494–1507.

Rusch, D. W., G. E. Thomas, W. McClintock, A. W. Merkel, S. M. Bailey, J. M. Russell III, C. E. Randall, C. Jeppesen, and M. Callan (2009), The cloud imaging and particle size experiment on the Aeronomy of Ice in the Mesosphere mission: Cloud morphology for the northern 2007 season, *J. Atmos. Sol.-Terr. Phys.*, *71*(3–4), 356–364, doi:10.1016/j.jastp.2008.11.005.

Russell, J. M., III, M. G. Mlynczak, L. L. Gordley, J. Tansock, and R. Esplin (1999), An overview of the SABER experiment and preliminary calibration result, in *Proceedings of the SPIE, 44th Annual Meeting*, vol. 3756, pp. 277–288, Denver, Colo., 18–23 July.

Russell, J. M., III, et al. (2009), Aeronomy of Ice in the Mesosphere (AIM): Overview and early science results (2009), *J. Atmos. Sol.-Terr. Phys.*, *71*(3–4), 289–299, doi:10.1016/j.jastp.2008.08.011.

Salby, M. L. (1982a), Sampling theory for asynoptic satellite observations, part I, Space-time spectra, resolution and aliasing, *J. Atmos. Sci.*, *39*, 2577–2600.

Salby, M. L. (1982b), Sampling theory for asynoptic satellite observations, part II, Fast Fourier synoptic mapping, *J. Atmos. Sci.*, *39*, 2601–2614.

Schöch, A. (2007), Thermal structure and gravity waves in the Arctic middle atmosphere above ALOMAR (69.3°N, 16.0°E) , Ph.D. thesis, Leibniz-Institute for Atmospheric Physics, Kühlungsborn. (Available from http://www.iap-kborn.de/Thesis-Master-Diploma-PhD.64.0.html?&L=1).

Smith, A. K. (1983), Stationary waves in the winter stratosphere: seasonal and interannual variability, *J. Atmos. Sci.*, *40*, 245–261.

Smith, A. K. (1997), Stationary planetary waves in upper mesospheric winds, *J. Atmos. Sci.*, *54*, 2129–2145.

Tao, X., and C. S. Gardner (1995), Heat flux observations in the mesopause region above Haleakala, *Geophys.Res. Lett.*, *22*, 2829–2832.

Thayer, J. P., M. Rapp, A. J. Gerrard, E. Gudmundsson, and T. J. Kane (2003), Gravity wave influences on Arctic mesospheric clouds as determined by a Rayleigh lidar at Sondrestrom, Greenland, *J. Geophys. Res.*, *108*(D8), 8449, doi:10.1029/2002JD002363.

Thomas, G. E., and J. J. Olivero (1989), Climatology of polar mesospheric clouds 2. Further analysis of solar mesosphere explorer data, *J. Geophys. Res.*, *94*, 14,673–14,681.

Torrence, C., and G. P. Compo (1998), A practical guide to wavelet analysis, *Bull. Am. Meteorol. Soc.*, *79*(1), 61–78.

Turco, R. P., O. B. Toon, R. C. Whitten, R. G. Keesee, and D. Hollenback (1982), Noctilucent clouds: Simulation studies of their genesis, properties and global influences, *Planet. Space Sci.*, *30*, 1147–1181.

Walterscheid, R. L. (1981a), Dynamical cooling induced by dissipating internal gravity waves, *Geophys. Res. Lett.*, *8*, 1235–1238.

Witt, G. (1962), Height, structure, and displacements of noctilucent clouds, *Tellus*, *14*, 1–8.

Zhang, X., J. M. Forbes, M. E. Hagan, J. M. Russell III, S. E. Palo, C. J. Mertens, and M. G. Mlynczak (2006), Monthly tidal temperatures 20-120 km from TIMED/SABER, *J. Geophys. Res.*, *111*, A10S08, doi:10.1029/2005JA011504.

S. M. Bailey, Bradley Department of Electrical and Computer Engineering, Virginia Polytechnic Institute and State University, Blacksburg, VA 24061, USA.

A. Chandran, A. W. Merkel, D. W. Rusch, and G. E. Thomas, Laboratory for Atmospheric and Space Physics, University of Colorado, 1234 Innovation Drive, Boulder, CO 80303, USA. (chandran@lasp.colorado.edu)

S. E. Palo, Department of Aerospace Engineering, University of Colorado, Boulder, CO 80303, USA.

J. M. Russell III, Center for Atmospheric Sciences, Hampton University, Hampton, VA 23668, USA.

M. J. Taylor, Center for Atmospheric and Space Sciences and Physics Department, Utah State University, Logan, UT 84322, USA.